



The Growth of $\{1\ 1\ h\}\langle 1\ 2\ 1/h\rangle$ (α^* -Fiber) Grains and the Evanesce of $\{001\}\langle 100\rangle$ (Cube) Grains During the Recrystallization of Warm Rolled Fe-6.5 Wt Pct Si Non-oriented Electrical Steel

HAIJIE XU, YOULIANG HE, XUEDAO SHU, YUNBO XU, and STEVE YUE

$\langle 001\rangle//ND$ (normal direction) texture (including the cube, $\{001\}\langle 100\rangle$) is a desired final texture in non-oriented electrical steel (NOES) due to the alignment of two magnetically easy $\langle 100\rangle$ axes in the magnetization directions of the lamination core in rotating machines. However, after conventional rolling and annealing, the final texture of NOES is usually not the desired $\langle 001\rangle//ND$ texture, but the unfavorable $\langle 111\rangle//ND$ (γ -fiber), $\langle 110\rangle//RD$ (rolling direction) (α -fiber), and sometimes $\{1\ 1\ h\}\langle 1\ 2\ 1/h\rangle$ (α^* -fiber) textures. How do these textures (especially the α^* -fiber texture) form in the recrystallization process is still not completely understood. This paper investigates the recrystallization process of a warm rolled NOES containing 6.5 wt pct Si and tracks the growth of individual grains using a *quasi in-situ* EBSD (electron backscatter diffraction) technique. It is shown that the $\{1\ 1\ h\}\langle 1\ 2\ 1/h\rangle$ (α^* -fiber) grains (including $\{001\}\langle 120\rangle$, $\{114\}\langle 481\rangle$, and $\{112\}\langle 241\rangle$) normally form in the later stage of recrystallization, and mainly nucleate in the mid-thickness region of the deformed steel from grains having the $\langle 110\rangle//RD$ (α -fiber) orientations. Once nucleated, they can rapidly grow into the deformed matrix due to the large energy difference between the recrystallized and deformed grains and to the high-mobility grain boundaries with respect to the deformed matrix. On the other hand, although cube grains nucleate early during recrystallization, they cannot grow significantly into the deformed grains because of the very high misorientation angles with respect to the deformed grains, which may have caused “orientation pinning”. As a result, the cube grains are finally consumed by the large α^* -fiber grains due to size disadvantage. The origins of the α^* -fiber grains and cube grains are also analyzed using the *quasi in-situ* EBSD data obtained in the early stages of annealing.

<https://doi.org/10.1007/s11661-024-07370-3>

© The Minerals, Metals & Materials Society and ASM International 2024

I. INTRODUCTION

Fe-6.5 wt pct Si electrical steel shows superior magnetic properties such as low core loss and near-zero magnetostriction at high frequencies, and therefore is an

ideal soft magnetic material for electrical machines, especially electric motors working at high frequencies.^[1] While the high silicon content contributes to the excellent magnetic properties, it also leads to the formation of brittle intermetallic phases (B2 and D0₃).^[2] Thus, Fe-6.5 wt pct Si electrical steel has poor workability at room temperature. As a result, thin steel sheets cannot be produced by cold rolling. Adding a warm rolling process before cold rolling can normally improve the workability and enable the production of thin sheets by cold rolling.^[3–5] Warm rolling can also be used to produce thin sheets without cold rolling. Regardless of the differences in initial microstructure/texture and rolling conditions, cold rolled bcc (body centered cubic) metals usually show $\langle 110\rangle//RD$ (α -fiber) and $\langle 111\rangle//ND$ (γ -fiber) textures. During annealing, the recrystallization behavior of the deformed grains with different orientations differs significantly, due to the different tendencies to forming substructures in the deformed grains, and to the

HAIJIE XU and XUEDAO SHU are with the Zhejiang Provincial Key Laboratory of Part Rolling Technology, Faculty of Mechanical Engineering and Mechanics, Ningbo University, Ningbo 315211, Zhejiang, P.R. China. Contact e-mail: xuhaijie@nbu.edu.cn. YOULIANG HE is with the CanmetMATERIALS, Natural Resources Canada, Hamilton ON, L8P 0A5, Canada. Contact e-mail: youliang.he@nrcan-rcan.gc.ca. YUNBO XU is with the State Key Laboratory of Rolling Technology and Automation, Northeastern University, Shenyang 110819, P.R. China. STEVE YUE is with the Department of Materials Engineering, McGill University, Montreal, QC, H3A 2B2, Canada
Manuscript submitted August 29, 2023; accepted March 6, 2024.

Article published online March 25, 2024

difference in stored energy accumulated during cold deformation.^[6–13] Substructures (especially shear bands) are frequently seen in $\langle 111 \rangle // \text{ND}$ deformed grains, due to the high Taylor factors of these grains. The substructures provide preferred nucleation sites at the early stage of recrystallization.^[14] For example, Goss ($\{110\}\langle 001 \rangle$) grains prefer to nucleate in the shear bands of $\langle 111 \rangle // \text{ND}$ grains.^[12,15] On the other hand, the Taylor factors of the $\langle 110 \rangle // \text{RD}$ (α -fiber) grains are relatively low, so these grains are commonly featured by a more homogeneous strain distribution after deformation, a lower stored energy (and fewer geometrically necessary dislocations) and a lower lattice curvature,^[16] which usually recrystallize later than the $\langle 111 \rangle // \text{ND}$ grains.^[17] The $\langle 110 \rangle // \text{RD}$ deformed crystals are normally the final grains to be consumed during the recrystallization process.

The recrystallization of deformed $\langle 110 \rangle // \text{RD}$ grains, either in non-oriented or grain-oriented electrical steels, has been reported to form the α^* -fiber texture ($\{1\ 1\ h\}\langle 1\ 2\ 1/h \rangle$).^[10,11,18–23] The α^* -fiber is roughly parallel to the α -fiber in the $\varphi_2 = 45$ deg section of Euler space (Bunge notation) with $\varphi_1 \approx 20$ deg, extending from $\{001\}\langle 120 \rangle$ ($\varphi_1 = 18.4$ deg, $\Phi = 0$ deg), $\{114\}\langle 481 \rangle$ ($\varphi_1 = 19.5$ deg, $\Phi = 19.5$ deg), $\{113\}\langle 361 \rangle$ ($\varphi_1 = 20.2$ deg, $\Phi = 25.2$ deg) to $\{112\}\langle 241 \rangle$ ($\varphi_1 = 22.2$ deg, $\Phi = 35.2$ deg). This fiber texture has been observed in ferritic steels^[24] as well as in Fe–Si alloys after hot-band annealing,^[5] or after final annealing.^[5,23,25] The α^* -fiber texture (except the $\{001\}\langle 120 \rangle$ component) is not an ideal final texture for electrical steel, as it does not have the easy $\langle 100 \rangle$ axis in the sheet plane.

The formation mechanism of the α^* -fiber (especially the $\{113\}\langle 361 \rangle$ and $\{114\}\langle 481 \rangle$ components) has been investigated by Gobernado *et al.*^[26] and Sanjari *et al.*^[22]. It was shown that $\{113\}\langle 361 \rangle$ deformation bands appeared in fragments of the $\{001\}\langle 110 \rangle$ matrix during cold rolling, and served as the $\{113\}\langle 361 \rangle$ nuclei during annealing. Using ALAMEL theory, Gobernado *et al.*^[28] reported that fragmentation of the metastable $\{001\}\langle 110 \rangle$ grains occurred after 90 pct cold rolling, within which the α^* -texture formed. Through experiments and simulations, Kestens *et al.*^[29] validated that the deformed $\{001\}\langle 110 \rangle$ texture promoted the α^* -fiber texture with CSL (Coincidence Site Lattice) of $\Sigma 27$ (31.6 deg $\langle 110 \rangle$) and $\Sigma 7$ (38.2 deg $\langle 111 \rangle$). In addition to the $\{001\}\langle 110 \rangle$ matrix, Sanjari *et al.*^[27] also showed the recrystallization of the $\{113\}\langle 361 \rangle$ grains from the $\{001\}\langle 130 \rangle$ deformed grains. Zhang *et al.*^[20] reported that α^* -fiber grains nucleated in the $\{001\}\langle 110 \rangle$ – $\{112\}\langle 110 \rangle$ deformed matrix and showed growth advantage during recrystallization, which was also confirmed by Veberken *et al.*^[30]. In our previous work, the nucleation of the $\{001\}\langle 120 \rangle$ and $\{113\}\langle 361 \rangle$ grains was observed in the deformed $\{112\}\langle 110 \rangle$ grains in later stage recrystallization.^[5] These α^* -fiber grains also showed size advantage and led to strong final α^* -fiber texture. Thus, it has been generally accepted that the α^* -fiber texture is originated from the $\langle 110 \rangle // \text{RD}$ deformed matrix. However, how exactly the α^* -fiber grains grow during the recrystallization process is still not clear. On the other hand, it has been reported that in

early-stage recrystallization, cube crystals can nucleate in the recrystallized microstructure, but they rarely grow to form a major texture in the final material. The reason for the evanescence of cube grains during recrystallization is not known.

Several studies^[26–30] have been carried out to elucidate the recrystallization mechanism of $\{113\}\langle 361 \rangle$ and $\{114\}\langle 481 \rangle$ grains in $\langle 110 \rangle // \text{RD}$ deformed matrix of Fe–Si alloys by EBSD and transmission electron microscopy (TEM). However, these investigations mainly focused on the recrystallization of cold-rolled materials, which were not the same as the steel after warm rolling. On the other hand, most of those investigations could not follow the nucleation and growth of the same crystals during the recrystallization process. In this work, a *quasi in-situ* EBSD technique is utilized to track the recrystallization process of a warm rolled, Fe–6.5 wt pct Si steel, with focus on the growth of the $\{1\ 1\ h\}\langle 1\ 2\ 1/h \rangle$ (α^* -fiber) crystals in the deformed $\langle 110 \rangle // \text{RD}$ grains and the evanescence of cube grains nucleated in the early stage of recrystallization. It is intended to shed some light on the formation mechanism of the α^* -fiber texture during the recrystallization of warm rolled high silicon electrical steel.

II. MATERIAL AND EXPERIMENTAL PROCEDURE

The Fe–6.5 wt pct Si alloy investigated in this study consists of (wt pct): 0.009 C, 6.5 Si, 0.011 Mn, 0.005 Al, 0.005 S and 0.0002 N. The alloy was melted in a vacuum induction furnace and cast into a cylindrical ingot ($\Phi 100$ mm \times 180 mm), which was then forged into a billet with a thickness of 70 mm. After reheating to 1200 °C and holding for 30 minutes, the billet was hot rolled to a plate of 2.0 mm (thickness) in a laboratory reversing rolling mill. A rectangular plate of 85 mm \times 75 mm (length \times width) was cut and warm rolled to 1.2 mm (40 pct reduction) at 650 °C and further rolled to 0.5 mm (58 pct reduction) at 450 °C. The first warm rolling was carried out at a higher temperature to improve the workability of the steel by straining so that it can be warm rolled further at a lower temperature. After warm rolling, small samples were cut from the initial hot band and the warm rolled sheets, and the microstructures were characterized by optical microscopy (OM). The OM samples were prepared by grinding, polishing, and etching with a copper sulfate solution (5 g CuSO_4 + 25 ml HCl + 25 ml H_2O). A small specimen of 10 mm \times 8 mm \times 0.5 mm (RD \times TD \times ND) was cut and clamped between two stainless steel plates (5 mm in thickness) to facilitate sample preparation for EBSD characterization (Figure 1). The area to be examined was on the RD–ND plane.

The nucleation and growth of new crystals from the deformed microstructure were traced using EBSD techniques by interrupting the annealing process of the same specimen at different times (but at the same temperature). Since heavily deformed steel was difficult to index in EBSD (due to the large number of dislocations and lattice distortion), the specimen was first annealed at

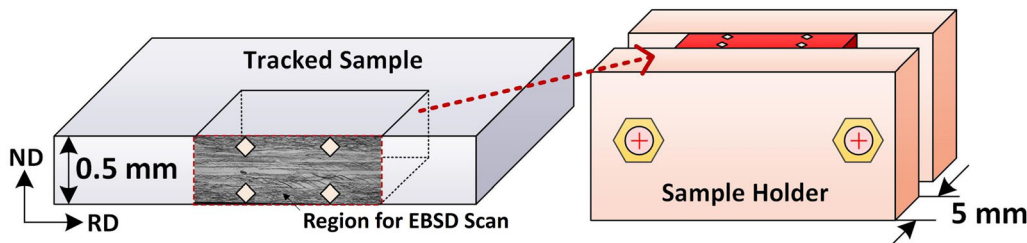


Fig. 1—Schematic illustration of the region to be examined as marked by microhardness indents and the sample holder for annealing experiments and EBSD characterization.

750 °C for 4 minutes before EBSD scan. The clamped sample was ground and polished using conventional metallographic procedures. It was finally polished using a 0.05 μm colloidal silica suspension for ~ 30 minutes. An area of 600 $\mu\text{m} \times 500 \mu\text{m}$ (RD \times ND) was marked on the specimen by microhardness indents to facilitate the subsequent tracking on the same region. EBSD scans were performed in a field emission gun scanning electron microscope (Nova NanoSEM, FEI) equipped with an EDAX OIM 6.2 EBSD system. An accelerating voltage of 20 kV and a step size of 0.35 μm were used for the EBSD scans. In addition to the initial EBSD scan after 4 minutes at 750 °C, a total of six more EBSD scans were obtained after annealing for various times (10 to 160 minutes) at the same temperature (750 °C) to trace the recrystallization process. It should be noted that, final annealing of NOES is normally conducted at 650 °C to 1050 °C for times from a few seconds to a few hours.^[3–5,7,8,12] A relatively low temperature of 750 °C is selected in this study to facilitate the tracking of the recrystallization process since recrystallization completes very fast at high temperatures and is difficult to track. To effectively trace the grain growth process, the annealing time is extended to 160 minutes in this study.

During the annealing experiments, the clamped sample was inserted into a tube furnace preheated at 750 °C in an argon atmosphere, and held for the accumulated times of 10, 20, 33, 48, 115 and 160 minutes. After reaching the designated holding times, the sample was quickly quenched to cold water to freeze the microstructure and prevent oxidation. After slight polishing with a colloidal silica solution for 1–3 minutes, the same area was examined under EBSD again. Because of the removal of the material by this polishing step (normally less than 1 μm from the surface), the grain boundaries after each interrupted annealing may not be exactly the same as the previous scan, but it is assumed to have a minimal effect on the tracing of the microstructure. The texture was represented by orientation distribution functions (ODF's), which were calculated using a harmonic series expansion method with a series rank of 22 and a Gaussian half width of 5 deg. A 15 deg deviation from the exact orientation was allowed when calculating specific grain orientations or texture fibers.

III. RESULTS

A. Microstructures After Hot Rolling and Warm Rolling

The microstructure after hot rolling is heterogeneous across the thickness, *i.e.*, fine equiaxed grains near the surfaces caused by dynamic/static recrystallization and elongated grains in the central region due to plane-strain compression (Figure 2(a)). After warm rolling at 650 °C and 450 °C, the microstructure is somewhat inherited, but the surfaces are featured by fine, deformed grains and the central region consists of severely substructured grains. The deformation substructures in the central region vary significantly at the two warm-rolling temperatures. After warm rolling at 650 °C to 1.2 mm with a thickness reduction of 40 pct, numerous slip bands form net-shape structures within the deformed grains (Figure 2(b)), which has been attributed to the activation of additional slip systems (e.g., $\{112\}\langle 111 \rangle$ and $\{123\}\langle 111 \rangle$) to the most common $\{011\}\langle 111 \rangle$ slip systems due to the relatively high deformation temperature.^[23] A common result of the activation of multiple slip systems is cross slip, which could have left traces of the slip planes on the surfaces. When the sample was further warm rolled at 450 °C with ~ 60 pct thickness reduction, such slip bands were significantly reduced. On the other hand, shear bands are formed (Figure 2(c)), similar to cold rolling.

B. Overall Microstructure and Texture Evolution During Annealing

The microstructure of the tracked region during annealing at 750 °C for various times is shown in Figure 3. Since the EBSD scans are performed on the same region, the evolution of individual grains can be tracked when the annealing time is extended. Generally, the surface regions recrystallize faster than the central region, as can be seen from the much larger number of recrystallized crystals at the beginning (after 10 minutes) and the larger area fractions of recrystallized grains in the surface regions than in the central region at all the times (see Figure 4(a)). This is because the surface regions have been subjected to large shear strain (due to the friction between the rolls and the steel sheet), which leads to high stored strain energy. The large driving force results in fast recrystallization upon annealing. On the other hand, due to the small grain size after warm rolling, plenty of grain boundaries and nucleation sites

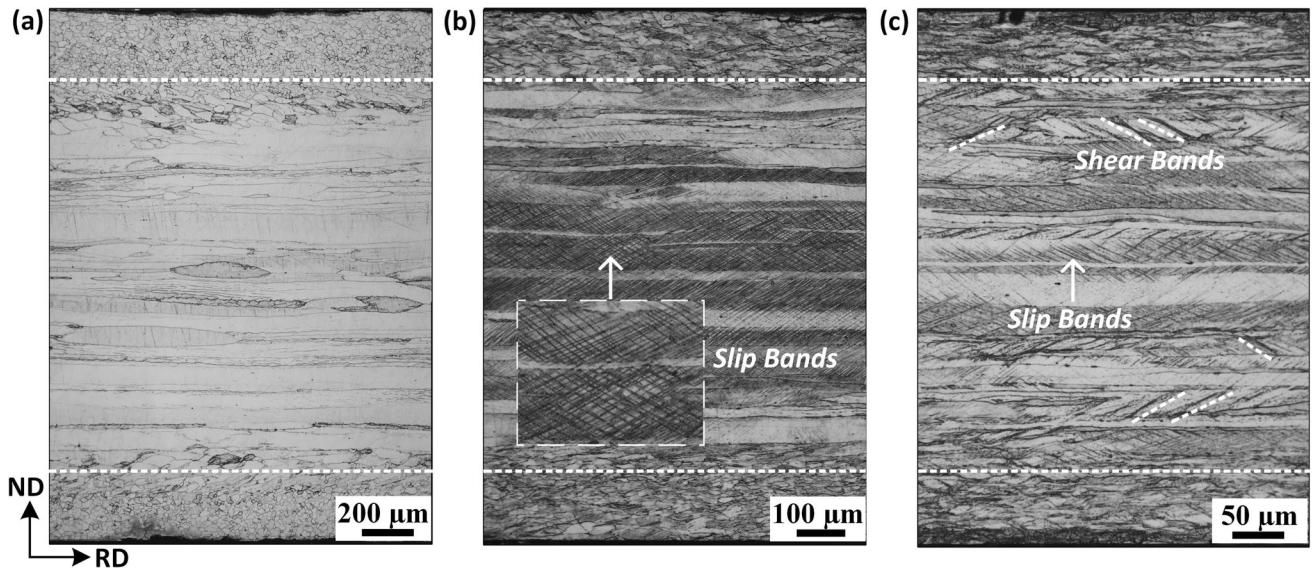


Fig. 2—Optical micrographs of the Fe-6.5 wt pct Si steel after: (a) hot rolling, (b) warm rolling at 650 °C (40 pct thickness reduction), and (c) warm rolling at 450 °C (~60% thickness reduction).

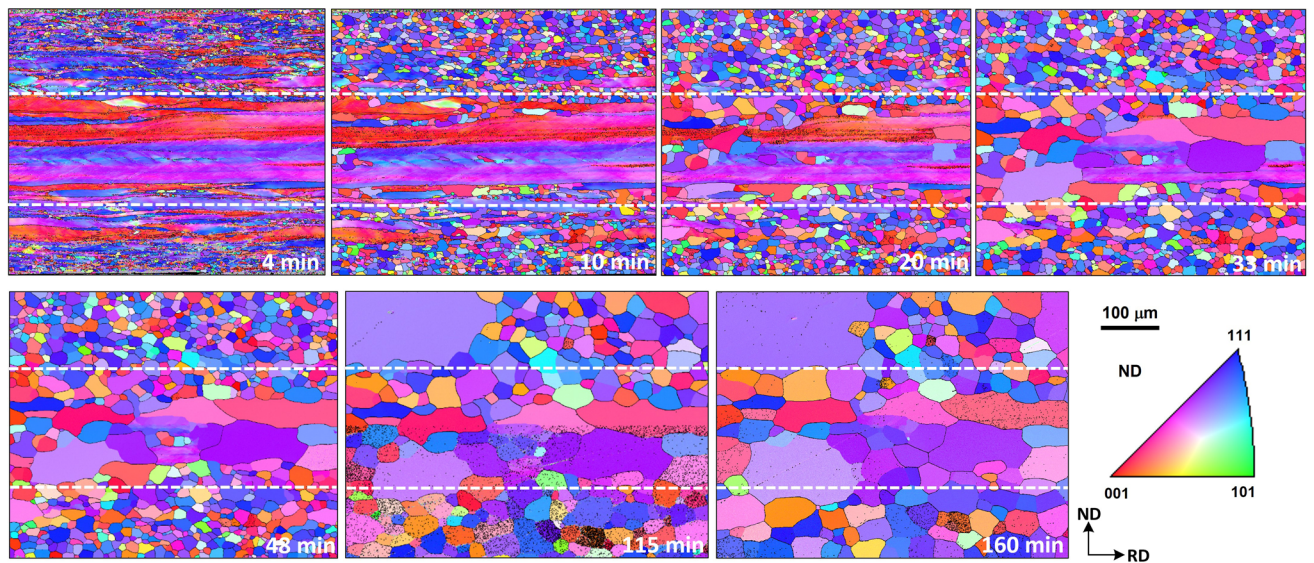


Fig. 3—The evolution of microstructure during annealing at 750 °C for different times as tracked by *quasi in-situ* EBSD on an area across the thickness of the warm rolled electrical steel sheet.

are available, which also promote recrystallization. Apparent nucleation in the central region is noticed after 20 minutes, at which considerable grain growth in the surface regions has also occurred. Recrystallization is essentially complete after 33 and 48 minutes for the surface and central regions, respectively. When the annealing time is extended to 115 minutes, abnormal grain growth in the surface region is observed. Further extending the annealing time to 160 minutes only leads to very small changes in microstructure.

At early-stage recrystallization, the nuclei in both the surface and central regions are very small and their average sizes are essentially the same (Figure 4(b)). Once the new crystals start to grow (i.e., after 20 minutes), the

average size of the recrystallized grains in the central region is always larger than that of the surface regions, indicating a larger growth rate in the central region. This is because the number of nuclei in the central region is much smaller than that in the surface regions. The growth of the new grains in the central region is mainly accomplished by the consumption of the deformed matrix, which has higher stored energy than the recrystallized grains (and thus larger driving force). In the surface regions, however, the driving force for growth is smaller since most of the grains have already recrystallized. The smaller average grain size in the surface regions is also due to the larger number of nuclei created during the early stage of recrystallization.

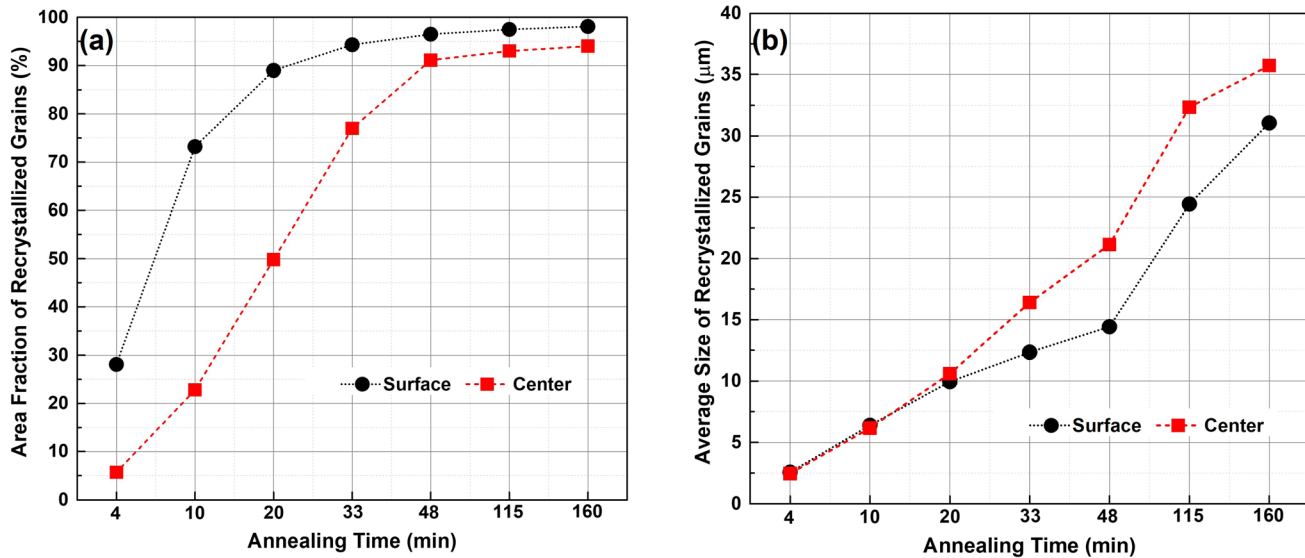


Fig. 4—The difference in the rate of recrystallization and average grain size between the surface and central regions during annealing at 750 °C for different times: (a) area fractions of the recrystallized grains, (b) average grain size of the recrystallized grains. Recrystallized and deformed grains are distinguished by grain orientation spread (GOS): grains with GOS < 3 deg are considered as recrystallized grains.

The evolution of the microtexture of the tracked region (the ND-RD cross section as shown in Figure 3) is shown in Figure 5(a). As the EBSD scan covers the entire thickness, the texture is a mixture of those at both the surface and center layers (Figure 5(b) and (c)).^[23] After warm rolling, the surface texture is mainly composed of a γ -fiber and an α -fiber (Figure 5(b)), but the intensities are quite low (around 6). The center layer (Figure 5(c)) shows a very strong α -fiber texture (intensities >30) and a relatively strong $\{111\}\langle 110 \rangle$ texture (intensity ~ 9). The very strong texture in the center layer is due to the very large elongated grains with almost single orientations (mainly $\{001\}\langle 110 \rangle$ and $\{112\}\langle 110 \rangle$).

From the microstructure shown in Figure 3, it has been seen that annealing at 750 °C for 4 minutes only leads to very little recrystallization; thus, the texture is essentially the same as that after warm rolling, which consists of the typical α -fiber and γ -fiber. However, a $\langle 001 \rangle // \text{ND}$ fiber (θ -fiber, including cube) is also noticed, although the intensity is relatively low, which is not normally seen in non-oriented electrical steel after cold rolling. With the increase of annealing time, the maximum texture intensity gradually decreases (the texture is randomized) until after 115 minutes at which abnormal grain growth is noticed and the maximum texture intensity starts to increase again (Figure 5(a)). It is also noted that the θ -fiber texture is intensified when the annealing time increases from 20 to 48 minutes (Figure 5(d)); after 115 minutes, its volume fraction starts to decrease. The volume fraction of the γ -fiber generally decreases with the increase of annealing time, but it shows a slight increase after 33 minutes. The volume fraction of the α^* -fiber rapidly increases with the increase of annealing time, especially after 115 minutes (due to the abnormal growth of a $\{112\}\langle 241 \rangle$ grain in the surface region, as shown in Figure 3). The α -fiber, on

the other hand, gradually weakens; after 115 minutes, its volume fraction shows a slight increase. The final texture is characterized by a strong α^* -fiber (especially the $\{112\}\langle 241 \rangle$ component), a relatively strong α -fiber and a γ -fiber. The rotated cube on the α -fiber commonly seen in recrystallized bcc metals is not observed in the final texture; only components between $\{114\}\langle 110 \rangle$ and $\{111\}\langle 110 \rangle$ are noticed.

As mentioned before, an advantage of the *quasi in-situ* EBSD technique is its ability to trace the evolution of individual grains during the annealing process. It has been seen that, after warm rolling at 450 °C (Figure 2(c)), the surface regions consist of very small deformed grains with large stored strain energy, which recrystallize fast at the early stage of annealing, and are therefore difficult to be traced in the limited number of interrupted EBSD scans performed in this study. Thus, the focus is placed on the central region where the number of nuclei is small and the recrystallization is relatively slow, which enable better tracing of the nucleation and growth of individual grains during the annealing process.

C. Evolution of Microstructure and Microtexture in the Central Region

The nucleation and growth of new grains from the deformed matrix in the central region is shown in Figure 6. Here, grain orientation spread (GOS) is used to distinguish the recrystallized grains from the deformed grains. The GOS of recrystallized grains is considered to be lower than 3° , while that of deformed grains is higher than 3° . Four originally deformed (elongated) areas can be identified, which are marked as A, B, C and D, respectively. Areas B and C each shows an essentially single orientation, i.e., $\{112\}\langle 110 \rangle$ and $\{001\}\langle 110 \rangle$, respectively, whereas Areas A and D, which

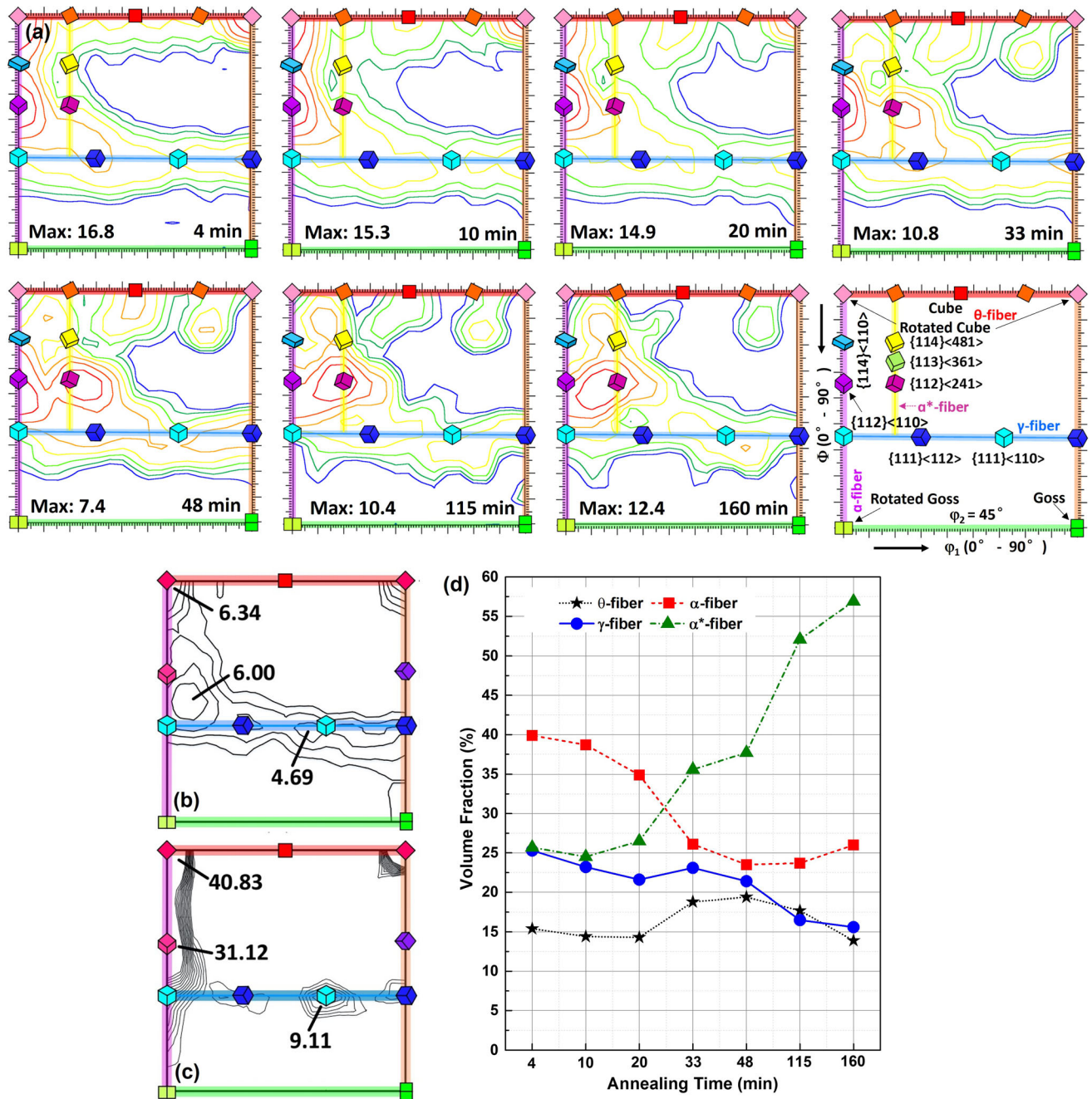


Fig. 5—The evolution of texture in the warm rolled steel: (a) microtextures at different times during annealing (corresponding to the microstructures shown in Fig. 3), (b) macrotexture of the warm rolled steel measured at the surface layer by XRD,^[23] (c) macrotexture measured at the center layer,^[23] (d) variations of the volume fractions of typical texture fibers with respect to the annealing time. $\varphi_2 = 45$ deg sections of the orientation distribution functions (ODF's) in Euler space (Bunge notation). Note that the sum of the volume fractions of the fibers may be greater than 100 Pct due to the allowed 15 deg deviation and to the overlapping of some texture components, e.g., $\{001\}\langle 110 \rangle$ is on both the θ -fiber and the α -fiber, $\{111\}\langle 110 \rangle$ is on both the α -fiber and γ -fiber, and $\{001\}\langle 120 \rangle$ is on both the θ -fiber and α^* -fiber.

are adjacent to the surface regions, contain multiple small, deformed grains (with $\{001\}$, $\{111\}$ and $\{112\}$ orientations for Area A, and $\{001\}$ and $\{111\}$ orientations for Area D).

At the beginning of recrystallization (*i.e.*, after the initial annealing for 4 minutes), some small nuclei are observed in Areas A and D, and there is no nucleation in the middle areas (B and C). The nuclei include various orientations such as Goss, cube, $\{111\}$, $\{112\}$, $\{114\}$,

$\{001\}$, etc. After 10 minutes, the new grains near the surface regions have grown slightly, and nucleation and grain growth have also been noticed in Area B. Some of the newly recrystallized grains show cube orientation, and some of these cube grains are relatively large as compared to other grains. In the meantime, relatively large $\{114\}\langle 481 \rangle$, $\{112\}\langle 241 \rangle$ and $\{111\}\langle 112 \rangle$ grains are also seen. A small $\{001\}\langle 120 \rangle$ grain (N1) is noticed in Area C ($\{001\}\langle 110 \rangle$).

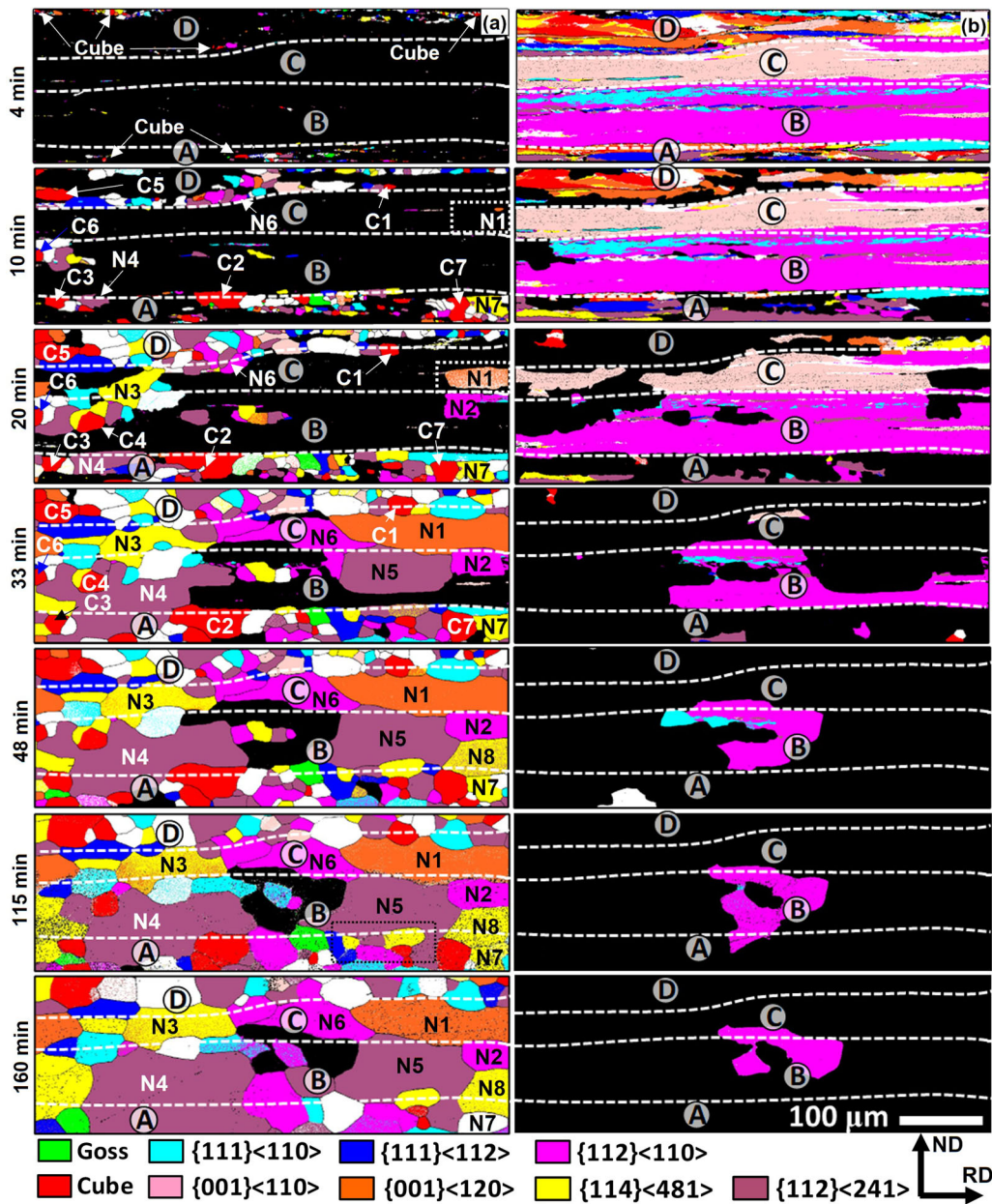


Fig. 6—Grain unique color maps showing the evolution of individual grains in the central region: (a) recrystallized grains, (b) deformed grains (Color figure online).

When the annealing time is increased to 20 minutes, the recrystallization is mostly complete in Areas A and D, and considerable recrystallization is also noticed in Areas B and C, but the majority remains unrecrystallized. The recrystallized grains (especially the cube grains) continue to grow. It is noticed that a recrystallized $\{112\}\langle 110 \rangle$ grain (N2) appears in Area B ($\{112\}\langle 110 \rangle$) and the $\{001\}\langle 120 \rangle$ grain (N1) grows considerably in Area C ($\{001\}\langle 110 \rangle$). A relatively large $\{114\}\langle 481 \rangle$ grain (N3) is also noticed in Area C. It should be noted that, grain N2 has similar orientation to the deformed $\{112\}\langle 110 \rangle$ matrix (Area B), which is unlikely a nucleation from the deformed matrix after the sample has been annealed for 20 minutes. This grain is

most probably a recrystallized grain that has already been formed (under the examined surface) during the previous steps and is revealed by the polishing steps at this moment. This can be confirmed by the fact that this grain essentially does not grow further after it is observed.

After 33 min, recrystallization in Areas B and C is almost complete, and N1 and N3 grow considerably. Grain N4 ($\{112\}\langle 241 \rangle$), which originated in Area A after 10 min, has also significantly grown. A new $\{112\}\langle 241 \rangle$ grain (N5) nucleates and grows significantly in Area B as well. A $\{112\}\langle 110 \rangle$ grain (N6), which originated in Area

D after 10 min, grows significantly into Area C ($\{001\}\langle 110\rangle$). On the other hand, the recrystallized grains in Areas A and D only slightly grow.

When the annealing time is further increased to 48 min, the unrecrystallized area is further reduced (only two deformed grains with orientations $\{112\}\langle 110\rangle$ and $\{111\}\langle 110\rangle$ are left). The large grains do not grow much during this period. The $\{114\}\langle 481\rangle$ grain (N7), which nucleated after 10 minutes in Area A, only slightly grows toward Area B. In the meantime, another $\{114\}\langle 481\rangle$ grain (N8) appears in Area B, which is right next to N7. Up to this point, the cube grains essentially remain in the microstructure.

After 115 minutes, although there is still a deformed $\{112\}\langle 110\rangle$ island remaining, the recrystallization is essentially complete and the growth of the recrystallized grains becomes very slow. The number of cube grains starts to decrease significantly and some cube grains have been consumed by other grains such as $\{112\}\langle 241\rangle$, $\{114\}\langle 481\rangle$ and $\{112\}\langle 110\rangle$.

After 160 minutes, grain growth continues, but the unrecrystallized island remains, although its size is further reduced. The cube grains have mostly evanesced and the large $\{112\}\langle 241\rangle$, $\{114\}\langle 481\rangle$, $\{001\}\langle 120\rangle$ and $\{112\}\langle 110\rangle$ grains in Areas B and C dominate the microstructure. It is thus seen that the deformed $\{112\}\langle 110\rangle$ grain (Region B) has been mainly transferred to $\{112\}\langle 110\rangle$ and $\{112\}\langle 241\rangle$ grains, and the deformed $\{001\}\langle 110\rangle$ grain (Region C) has been transferred to $\{001\}\langle 120\rangle$, $\{112\}\langle 110\rangle$ and $\{114\}\langle 481\rangle$ grains.

The changes of the area fractions of major recrystallized and deformed grains with respect to the annealing time are summarized in Figure 7. It is seen that, with the increase of the annealing time, the area fractions of both the recrystallized α^* -fiber ($\{001\}\langle 120\rangle$, $\{114\}\langle 481\rangle$, $\{112\}\langle 241\rangle$) and α -fiber ($\{112\}\langle 110\rangle$) grains generally increase (Figure 7(a)), while the area fraction of the cube grains first increases (from 4 to 10 minutes), then stabilizes from 20 to 115 minutes, and finally drops after 160 minutes. The area fractions of almost all the deformed grains decrease to almost zero after 33 minutes, except the $\{112\}\langle 110\rangle$ grains (Figure 7(b)), part of which (~ 6 pct) remains even after 160 minutes. Rapid growth of the recrystallized grains (and the consumption of the deformed grains) occurs during the period from 10 to 48 minutes.

The evolution of the overall texture of the central region is shown in Figure 8. The starting texture consists of a very strong α -fiber, with peaks at $\{112\}\langle 110\rangle$ and $\{001\}\langle 110\rangle$ (corresponding to Areas B and C, respectively), a minor γ -fiber and a weak $\langle 001\rangle//\text{ND}$ fiber. With the increase of the annealing time, the texture is generally randomized (maximum intensity decreases) due to the formation of the recrystallized grains with different orientations within the originally almost single-oriented grains (Areas B and C). Both the $\langle 001\rangle//\text{ND}$ fiber (including cube) and the α -fiber (including rotated cube and $\{112\}\langle 110\rangle$) weakens gradually when the deformed grains are replaced by recrystallized grains. The $\{112\}\langle 241\rangle$ component (on the α^* -fiber) starts to appear after 33 minutes and becomes the strongest

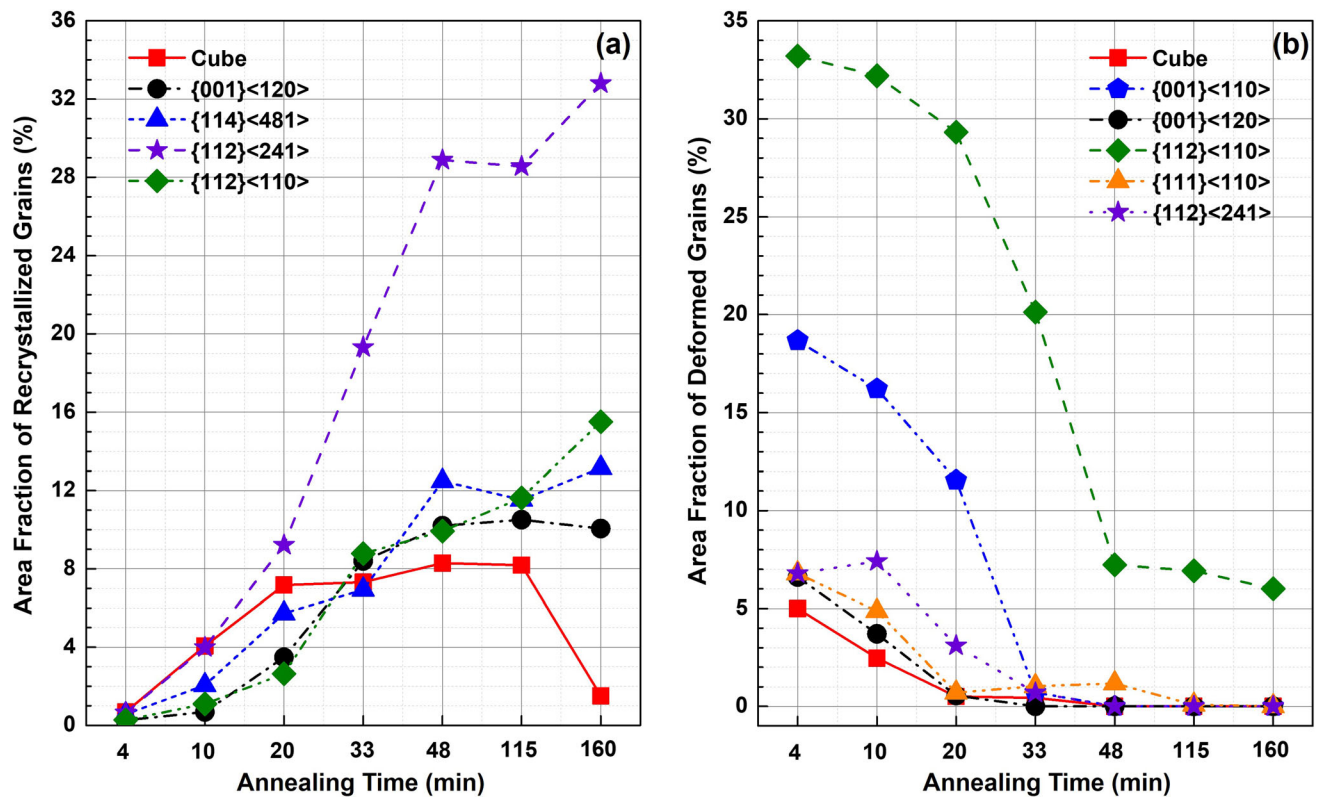


Fig. 7—The changes of area fractions of major orientations with respect to the annealing time: (a) recrystallized grains, (b) deformed grains.

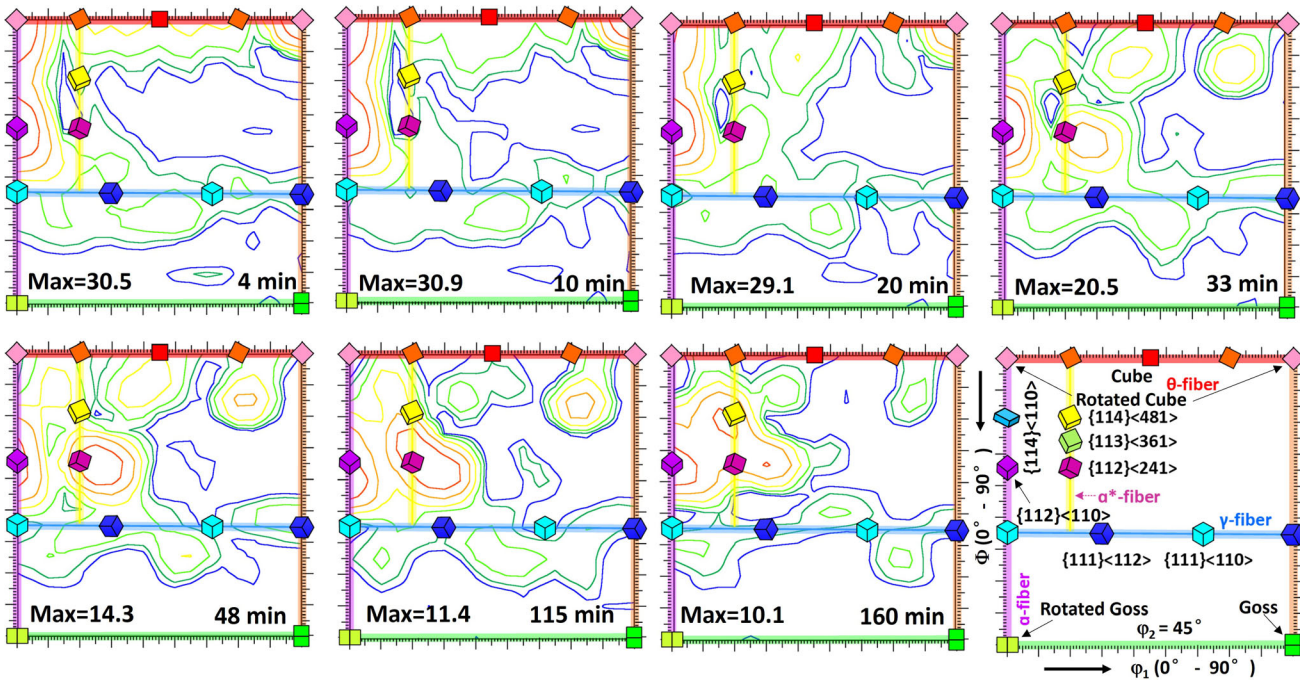


Fig. 8—The evolution of texture in the central region during annealing at 750 °C for different times. $\phi_2 = 45$ deg sections of the orientation distribution functions (ODFs) in Euler space (Bunge notation).

component after 48 minutes. The α^* -fiber and the $\{112\}\langle 110 \rangle$ component dominate the final texture after 160 minutes.

It should be noted that, since a relatively low temperature (750 °C) was used to anneal the steel and the annealing process was interrupted several times during the experiments, the final recrystallization textures may be different from those after annealing at a higher temperature for a shorter time. Compared to the macrotexture of the same steel after annealing at 1000 °C for 10 minutes (center layer),^[23] a much stronger $\{112\}\langle 110 \rangle$ texture is observed in this study, due to the retention of the $\{112\}\langle 110 \rangle$ grains even after 160 minutes annealing (Figure 6).

IV. DISCUSSION

Although many studies have been carried out trying to understand the recrystallization phenomena, the mechanisms governing the nucleation and grain growth during annealing and the formation of the final microstructure and texture are still not completely understood.^[31–34] Several investigations on the microstructure, texture, and mechanical properties of warm-rolled structural steels can be found in the literature,^[23,35–42] but only a few studies have been dedicated to the warm rolling of electrical steels.^[4,39,43,44] Although the microstructure and texture after warm rolling seem to be similar to those after cold rolling, i.e., exhibiting layered structures across the thickness and mainly consisting of the α - and γ -fiber textures,^[23,45,46] rolling at an elevated temperature has

shown apparently different effects on the deformed microstructure, stored energy, and texture as compared to cold rolling.^[23,39,40,47] The stored energy of the steel after cold rolling has been measured (by X-ray diffraction) to be in the order of $E_{\{110\}\langle 110 \rangle} \gg E_{\{111\}} \gg E_{\{110\}\langle 001 \rangle} \gg E_{\{112\}} \gg E_{\{001\}}$,^[48–50] while in warm rolled electrical steel, it is found that the stored energy is in the order of $E_{\{111\}} \gg E_{\{110\}} \gg E_{\{001\}} \gg E_{\{112\}}$.^[40] As a result, the recrystallization behavior of warm rolled electrical steel might be different from that after cold rolling. The nucleation of new grains from the deformed matrix is mainly determined by the stored energy and substructures of the deformed grains, while the growth of the recrystallized grains is significantly affected by the mobility of the grain boundaries. All of these are closely related to the orientations of the grains. The quasi in-situ EBSD data obtained in this study provide some direct and detailed information which is not available using conventional EBSD and thus make it possible to analyze the evolution of recrystallization in a quasi-dynamic way.

A. The Growth of the α^* -Fiber Grains

It has been shown in many studies that $\langle 111 \rangle // \text{ND}$ grains show large Taylor factors and tend to form shear bands after plane-strain compression. Shear bands are preferred nucleation sites for recrystallization due to their high stored energy. As a result, recrystallization is normally first observed in these areas (A and D) at the beginning of annealing (4 minutes). The grains in Areas B ($\{112\}\langle 110 \rangle$) and C ($\{001\}\langle 110 \rangle$) have smaller Taylor factors and lower stored energy than the $\langle 111 \rangle // \text{ND}$

grains; thus, they recrystallize later. Area C ($\{001\}\langle 110\rangle$) has the lowest tendency to form shear bands (lowest Taylor factor); thus, it lacks preferred nucleation sites to start recrystallization and is the last to recrystallize.

Once the nuclei are formed in the deformed microstructure, its growth is mainly controlled by the driving force and the boundary characteristics. According to classical recrystallization theory, the growth rate of a crystal is given by^[47,51]

$$\dot{G} = MP \approx 0.5M\rho Gb^2 \quad [1]$$

where M is the grain boundary mobility, P is the driving pressure (force) which is proportional to the dislocation density (ρ), G is the shear modulus and b is the Burgers vector. The mobility of the grain boundary is dependent on a few factors, e.g., temperature, boundary misorientation and structure, solute, precipitate, etc. Generally, the mobility of high-angle grain boundaries (HAGB) is higher than that of low-angle grain boundaries (LAGB), while the activation energy for boundary migration of HAGB is lower than that of LAGB.^[47]

It has been seen that, grain growth occurred rapidly during the period from 20 to 33 minutes, mainly in Areas B and C where the number of nuclei is small, and the growth speed of the recrystallized grains is high. In the meantime, recrystallized grains in Areas A and D only grow slightly since most of these areas have already recrystallized and the driving force for growth is small. In Areas B and C, however, the newly formed (very few) grains can rapidly grow due to the large energy difference (driving force) between the recrystallized and deformed grains, and to the high-angle grain boundaries (with high mobility) between the new grains and the deformed grains. The five large recrystallized grains in Areas B and C, i.e., N1 ($\{001\}\langle 120\rangle$), N3 ($\{114\}\langle 481\rangle$), N4 and N5 ($\{112\}\langle 241\rangle$), and N6 ($\{112\}\langle 110\rangle$), all rapidly grow into the deformed grains due to the large driving force and the HAGB with respect to the deformed grains. N1, N3 and N6 show misorientations of 18.4 deg $\langle 110\rangle$ (close to CSL $\Sigma 19a$, 26.5 deg $\langle 110\rangle$), 27.5 deg $\langle 543\rangle$ (close to CSL $\Sigma 13b$, 27.8 deg $\langle 111\rangle$) and 35.3 deg $\langle 110\rangle$ (close to CSL $\Sigma 27$, 31.6 deg $\langle 110\rangle$), respectively, with respect to Area C ($\{001\}\langle 110\rangle$), while N4 and N5 show a misorientation of 22.2 deg $\langle 112\rangle$ with respect to Area B ($\{112\}\langle 110\rangle$). These misorientations are all in the high-mobility HAGB range, i.e., 15 deg–40 deg. In addition, the number of nuclei in Areas B and C is much smaller than that in Areas A and D, which results in much larger grain sizes of the α^* -fiber grains.

When the annealing time is extended to 48 minutes or more, only the two $\{112\}\langle 241\rangle$ grains (N4 and N5) adjacent to Area B ($\{112\}\langle 110\rangle$) show some growth, again, due to the large difference in stored energy between the recrystallized and deformed grains, and to the high mobility of the HAGB. The growth of the other grains, e.g., N1, N3, and N6, is essentially retarded, either due to the surrounding grains being recrystallized already (N1 and N3), or the low mobility of very low misorientation angles (N6) with respect to the deformed matrix (the remaining $\{112\}\langle 110\rangle$ in Area B). Further

increasing the annealing time to 115 minutes results in very small changes, i.e., the shrinking of the final part of the deformed grain and the growth of a few grains by consuming the neighboring grains. After 160 minutes, most of the grains still remain unchanged, but the cube grains located near the large $\{112\}\langle 241\rangle$ and $\{114\}\langle 481\rangle$ grains are mostly consumed.

B. The Evanesce of Cube Grains

Cube is not a common recrystallization texture in BCC metals and is rarely reported to be a final texture in non-oriented electrical steel after conventional rolling and annealing (without phase transformation or secondary recrystallization). Nevertheless, cube texture has been developed in twin-roll cast^[52,53] or incline rolled^[12] non-oriented electrical steels. Cube grains have been claimed to nucleate in the deformation bands of the deformed $\{001\}\langle 120\rangle$ - $\{114\}\langle 148\rangle$ - $\{113\}\langle 136\rangle$ - $\{112\}\langle 241\rangle$ grains,^[52,53] as well as in the shear bands of $\{110\}\langle 110\rangle$ grains,^[12] all of them being after cold rolling. The formation of final cube texture in warm rolled 6.5 wt pct Si non-oriented electrical steel has not been seen in the literature.

In this study, although it is noted that cube grains do nucleate at the beginning of annealing in the warm rolled 6.5 wt pct Si steel, the growth of these grains is much slower than those of the α^* -fiber grains. The cube grains (C1–C4) that are adjacent to the same deformed grains (Areas B and C) do not grow into the deformed matrix even if the driving force is large (large difference in stored energy). An examination of the misorientations between these cube grains and the two deformed grains (Areas B and C) reveals that C2–C4 show an approximate misorientation of 56.6 deg $\langle 123\rangle$ with respect to B ($\{112\}\langle 110\rangle$) and C1 exhibits a misorientation of 45 deg $\langle 001\rangle$ with respect to C, both of them being out of the high-mobility misorientation angle range of 15 deg–40 deg. This may imply an “orientation pinning” effect as observed by some authors in Al^[54] and Cu.^[55] Since the cube grains cannot grow into the deformed matrix when competing with the α^* -fiber grains, they are finally consumed by the recrystallized α^* -fiber grains due to the size disadvantage, which results in the evanesce of the cube texture in the final microstructure. However, since grain boundary mobility is also highly dependent on the distribution, shape and size of the second-phase particles, it is also possible that the grain boundaries between cube and the two α -fiber orientations ($\{001\}\langle 110\rangle$ and $\{112\}\langle 110\rangle$) might favor the precipitation of particles, which may drag the motion of the grain boundaries. This, however, needs to be further verified, e.g., using advanced transmission electron microscopy.

The nucleation and growth of cube grains in 3.0 wt pct Si steel have been investigated by Takajo *et al.*^[15] using both in-situ and ex-situ EBSD techniques. Cube nuclei (originated in fragments of deformed $\{114\}\langle 481\rangle$ grains) were found to first grow inside the prior grain boundaries at a low temperature, and then beyond the boundaries at high temperatures due to size advantage. However, the growth of the cube grains did not continue beyond 750 °C, due to the possible pinning

of dislocations or solute drag at the grain boundaries. It was also observed that the cube grains were replaced by other grains if the annealing temperature was increased to 950 °C. It is thus seen that the mechanism governing the growth and evanesce of the cube grains is still not clear since both annealing for an extended time at a relatively low temperature (this study) and annealing at a high temperature for a short time^[15] can result in the evanesce of the cube grains. The proposed mechanism in this study, i.e., orientation pinning, may not be generalized as alternative mechanisms may also play a role in determining the evanesce of the cube texture in electrical steels.

It should be noted that the *quasi in-situ* EBSD technique employed in this study is not ideal for catching the nucleation process since nucleation occurs in a very short period of time and the interrupted EBSD scans obtained in this study might only capture the grains after growth. However, based on the EBSD scans at the early stage of annealing, a rough analysis of the formation of the common recrystallized grains in the final microstructure is possible. The following sections briefly discuss the formation of both the α^* -fiber grains and the cube grains at the early stage of annealing.

C. Formation of the $\{001\}\langle 120\rangle$ Grains

Figure 9 shows the formation and growth of a $\{001\}\langle 120\rangle$ grain (N1) during annealing. This grain appears in the deformed $\{001\}\langle 110\rangle$ matrix (Area C) after 10 minutes (Figure 6). It has been shown before that deformed $\{001\}\langle 110\rangle$ crystals have a small Taylor factor and usually there is no shear bands or deformation bands within these grains; thus, nucleation within deformed $\{001\}\langle 110\rangle$ grains is very unlikely, especially

in the microstructure after warm rolling at an elevated temperature and in the material that has already undergone initial annealing (4 minutes). Therefore, the $\{001\}\langle 120\rangle$ “nucleus” observed in Area C (after 10 minutes) might have come from a grain that has already nucleated in the initial annealing but is located under the scanned surface and not revealed by the previous scan (after 4 minutes). After 10 minutes, it grows into the deformed $\{001\}\langle 110\rangle$ grain and is revealed by the scan. The misorientation of this new grain with respect to the deformed matrix is 18.4 deg $\langle 001\rangle$, which is a high-angle grain boundary and has high mobility; thus, it can grow quickly into the deformed matrix.

D. Formation of the $\{114\}\langle 481\rangle$ Grains

Several authors^[10,11,18–20,22,26,56] have investigated the formation of the α^* -fiber grains (mainly $\{113\}\langle 361\rangle$ and $\{114\}\langle 481\rangle$) during the annealing of bcc metals (including Fe–Si alloys). The origin of these grains has been attributed to the deformed $\{001\}\langle 110\rangle$ grains (normally after heavy cold rolling, i.e., >95 pct thickness reduction),^[26] and to the deformed $\{112\}\langle 110\rangle$ grains.^[20,30] The formation of the α^* -fiber texture has been attributed to the 26.5 deg $\langle 110\rangle$ misorientation (Σ 19a CSL boundary) between the deformed $\{112\}\langle 110\rangle$ grain and the recrystallized $\{113\}\langle 361\rangle$ and $\{114\}\langle 481\rangle$ grains, which enhances the mobility of the grain boundary.^[57]

One nucleation site of the $\{114\}\langle 481\rangle$ grains observed in this study is within the shear bands of deformed $\{112\}\langle 110\rangle$ grains, as shown in Figure 10. $\{112\}\langle 110\rangle$ grains show a relatively high Taylor factor, and shear bands frequently form in these grains. Recrystallized $\{114\}\langle 481\rangle$ grains (G3 and G4) appear after annealing for 10 minutes, and then grow to consume the

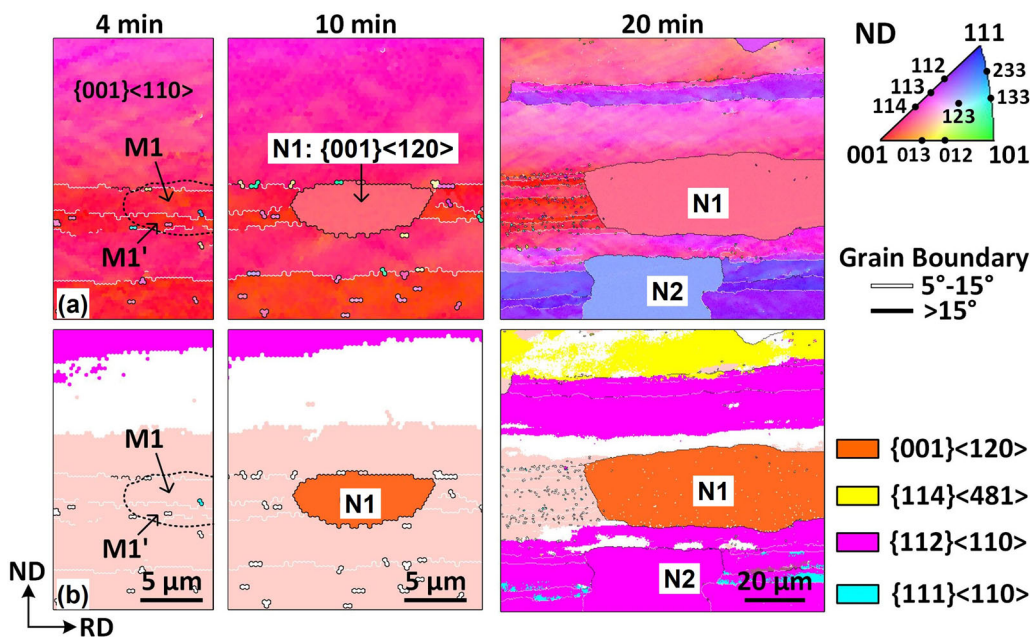


Fig. 9—The formation of a $\{001\}\langle 120\rangle$ grain during early-stage annealing: (a) inverse pole figure maps, (b) grain unique color maps. Note that the sudden change of the orientations (from 10 to 20 min) in the bottom part is due to the revealing of the recrystallized $\{112\}\langle 110\rangle$ grain (N2) at this moment by repolishing of the sample (see Section III–C) (Color figure online).

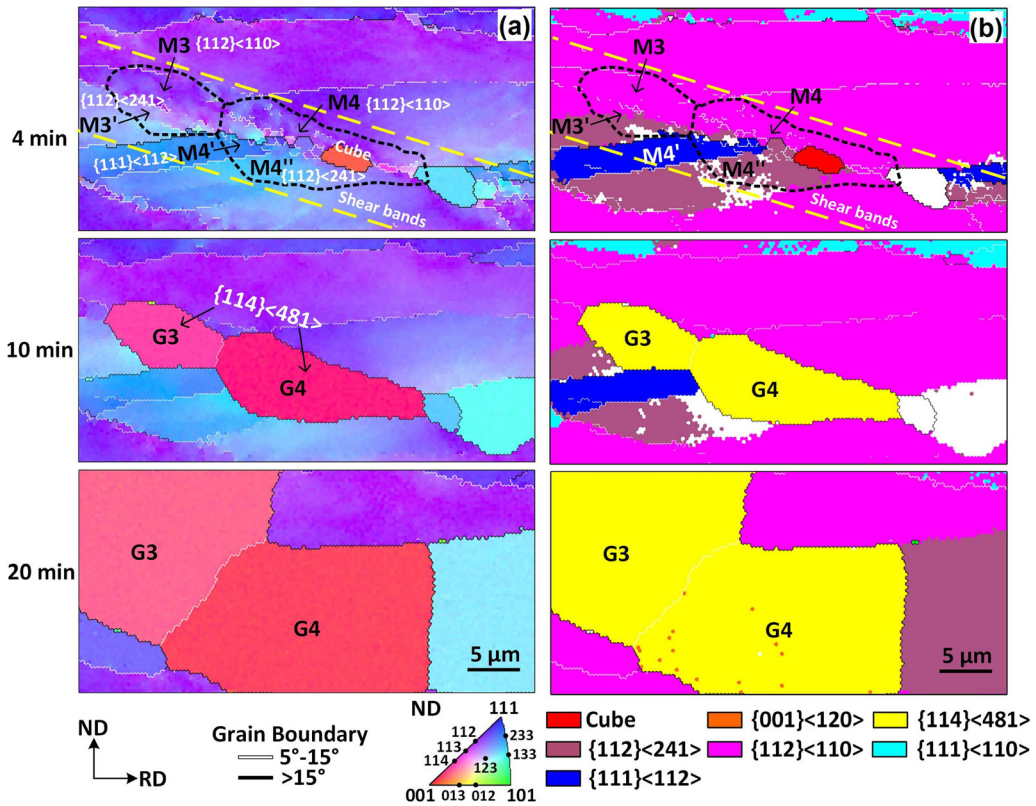


Fig. 10—The formation of $\{114\}\langle 481\rangle$ grains during early-stage annealing: (a) inverse pole figure maps, (b) grain unique color maps (Color figure online).

surrounding deformed matrix. $\{114\}\langle 481\rangle$ grains show misorientations of 16 deg, 25 deg and 37 deg with respect to the $\{112\}\langle 241\rangle$, $\{112\}\langle 110\rangle$, and $\{111\}\langle 112\rangle$ grains, respectively. These misorientations are all high-mobility HAGBs.

E. Formation of the $\{112\}\langle 241\rangle$ Grains

In the literature, the α^* -fiber normally refers to orientations from $\{114\}\langle 481\rangle$ to $\{113\}\langle 361\rangle$. In this study, the $\{112\}\langle 241\rangle$ orientation, which may be regarded as an extension of the normal α^* -fiber, seems to be the orientation that shows obvious growth advantage over other grains. It has been shown before that large $\{112\}\langle 241\rangle$ grains remain in the final microstructure after annealing for 160 minutes (Figures 3 and 6), leading to a strong recrystallized $\{112\}\langle 241\rangle$ texture. $\{112\}\langle 241\rangle$ grains are seen nucleating in the shear bands of deformed $\{111\}\langle 110\rangle/\{112\}\langle 110\rangle$ grains, as shown in Figure 11. These grains do not appear until after annealing for 10 or 20 minutes. The orientations of the recrystallized $\{112\}\langle 241\rangle$ grains are close to those of the corresponding deformed matrix from which they nucleate, i.e., G9 shows a misorientation of ~ 9.0 deg to M9 and M9', G10 a ~ 15.0 deg misorientation to M10, and G11 a misorientation

of ~ 12.5 deg to M11. This is similar to the nucleation of $\langle 111\rangle//\text{ND}$ grains in the shear bands of the deformed $\langle 111\rangle//\text{ND}$ grains as has been observed in many studies in the literature.

F. Formation of the $\{001\}\langle 100\rangle$ (Cube) Grains

In cold-rolled electrical steels, recrystallized cube crystals have been reported to nucleate from different sites depending on the processing method and the annealing conditions, including: (1) cube ($\{001\}\langle 100\rangle$) deformation bands and shear bands of $\{111\}\langle 110\rangle$ grains,^[52] (2) fragments of deformed $\{114\}\langle 148\rangle$ grains,^[15] (3) shear bands of rotated Goss,^[12,58] (4) $\{114\}\langle 481\rangle$ and $\{112\}\langle 241\rangle$ deformation bands and shear bands within the $\{114\}\langle 110\rangle$, $\{112\}\langle 110\rangle$ and $\{111\}\langle 112\rangle$ matrix.^[53] As has been seen in Figure 3, initial cube nuclei appear early during annealing (after 4 minutes), but these grains are very small and can barely be noticed. After 10 minutes, many cube grains are observed in Areas A and D, some being quite large already, e.g., C2, C5 and C7 (Figure 6). A close examination of their neighboring grains (Figure 12) reveals that some of the cube grains are located near the deformed $\{111\}\langle 112\rangle/\{112\}\langle 110\rangle$ grains (C1), and some near $\{001\}\langle 100\rangle/\{114\}\langle 481\rangle/\{112\}\langle 110\rangle/\{112\}\langle 241\rangle$

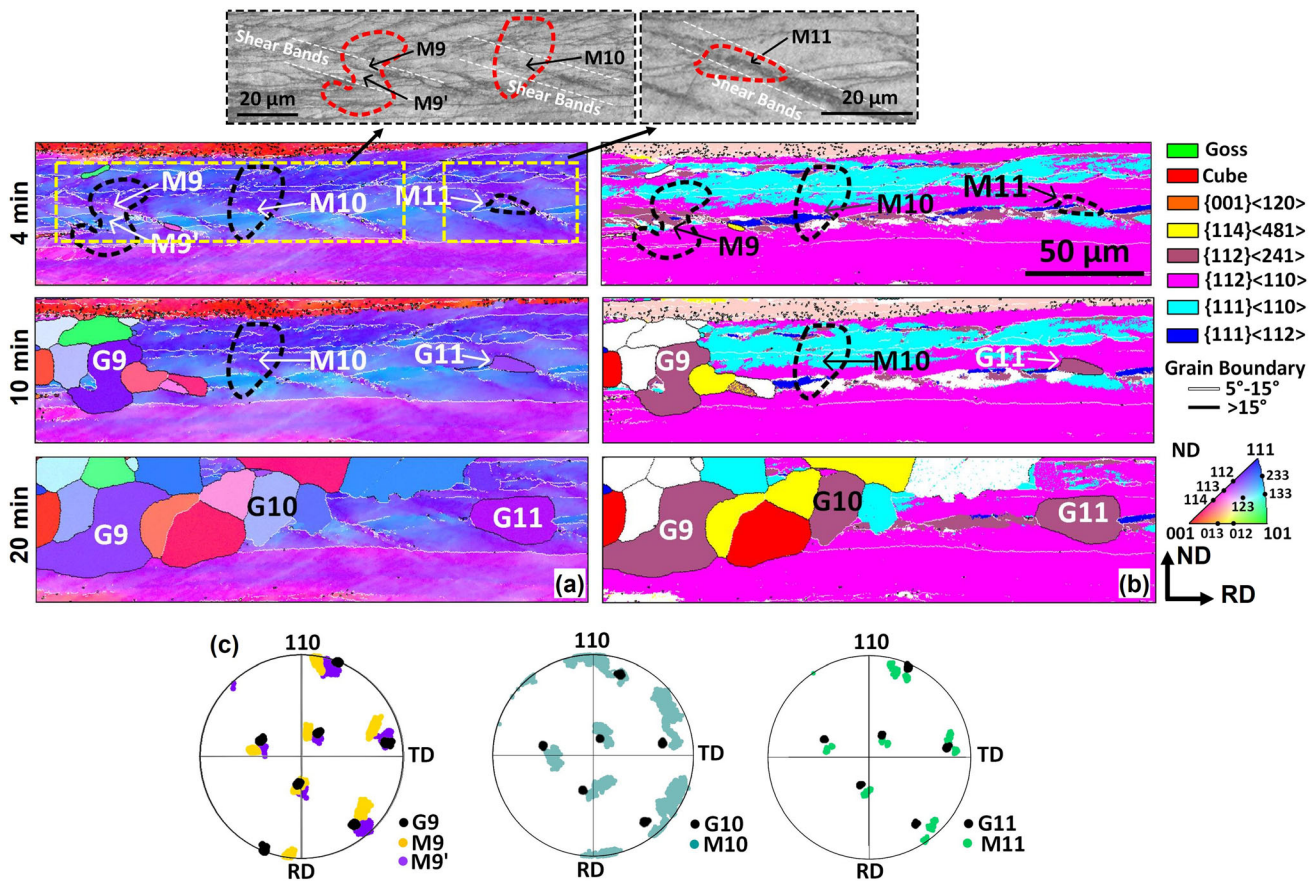


Fig. 11—The formation of $\{112\}\langle 241\rangle$ grains during early-stage annealing: (a) inverse pole figure maps, (b) grain unique color maps, (c) pole figures of the $\{112\}\langle 241\rangle$ grains and their neighbors.

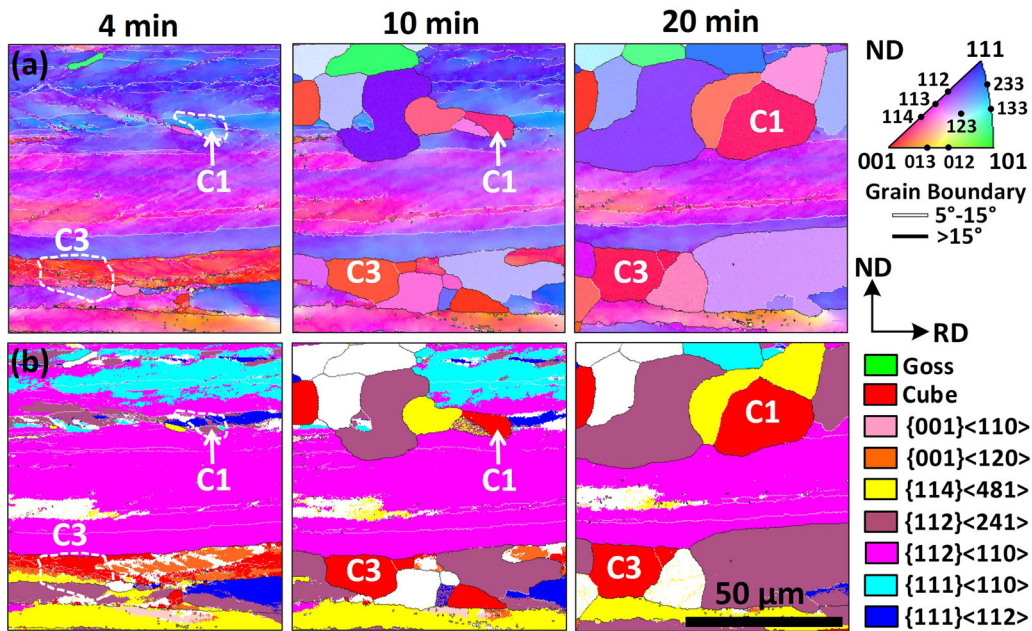


Fig. 12—The formation of $\{001\}\langle 100\rangle$ (cube) grains during early stage annealing: (a) inverse pole figure maps, (b) grain unique color maps (Color figure online).

grains (C3). All these nucleation sites have already been observed by others in the literature. It should be noted that nucleation of a cube crystal (C4 in Figure 6) in Area B ($\{112\}\langle 110\rangle$) has also been noticed, but cube is not seen to nucleate within the deformed $\{001\}\langle 110\rangle$ grain (Area C).

From the above analysis of the formation of various grains it is seen that the exact nucleation sites of these grains are very difficult to identify as the nuclei are adjacent to grains or parts of grains with different orientations (orientation gradient due to deformation). When the nuclei are large enough to be captured by EBSD, they may have already grown, and it is difficult to determine the exact origin of the nuclei as the neighboring orientations are mostly different with each other as well. Thus, the *quasi in-situ* EBSD technique used in this study is not ideal for the identification of nucleation, but rather for the tracking of individual grain growth.

V. SUMMARY AND CONCLUSIONS

The recrystallization of an Fe-6.5 pct Si non-oriented electrical steel after warm rolling was investigated using a *quasi in-situ* EBSD technique. The evolution of individual grains during the recrystallization process was tracked and analyzed. The results can be summarized as follows:

- In the central region of the steel sheet, very few but very large α^* -fiber ($\{001\}\langle 120\rangle$, $\{114\}\langle 481\rangle$ and $\{112\}\langle 241\rangle$) and $\{112\}\langle 110\rangle$ (α -fiber) grains are seen to rapidly grow during annealing and form the final major texture.
- The rapid growth of the α^* -fiber and $\{112\}\langle 110\rangle$ grains are due to the large difference in the stored energy between the recrystallized and deformed grains, and to the high-mobility of high-angle grain boundaries in the range of 15 deg–40 deg. Grains with the same orientation as the deformed matrix cannot grow due to the low mobility of the grain boundaries.
- Cube grains nucleate early during recrystallization, but their growth into the deformed matrix is retarded, probably due to the “orientation pinning” effect as observed in the recrystallization of fcc metals. Because of size disadvantage, the cube grains are mostly consumed by the large $\{112\}\langle 241\rangle$ grains and finally evanesce.
- The exact nucleation sites of various grains cannot be unequivocally determined using the *quasi in-situ* EBSD technology since it is very difficult to capture the exact nucleation moment during the recrystallization process.

ACKNOWLEDGMENTS

This work was financially supported by National Natural Science Foundation of China (No. 52205385), Ningbo Science and Technology Plan Project (Nos.

2021J098 and 2020Z110). Y. H. acknowledges the financial support from Natural Resources Canada through the Program of Energy Research and Development (PERD). H. X. is grateful to the support from Chinese Scholarship Council (No. 201806080099). The authors are grateful to Jian Li and Renata Zavadil for assistance in EBSD characterization.

AUTHOR CONTRIBUTION

Haijie Xu: Conceptualization, Investigation, Writing—original draft. Youliang He: Conceptualization, Resources, Writing—review & editing, Funding acquisition. Xuedao Shu: Supervision, Resources, Writing—review & editing, Funding acquisition. Yunbo Xu: Project administration, Supervision, Funding acquisition. Steve Yue: Supervision, Resources, Funding acquisition.

DATA AVAILABILITY

The raw/processed data required to reproduce these findings cannot be shared at this time due to technical or time limitations.

COMPETING INTEREST

There are no known competing financial interests or personal relationships that could have appeared to influence the work reported in this paper.

REFERENCES

1. G. Ouyang, X. Chen, Y. Liang, C. Maczewski, and J. Cui: Review of Fe-65 wt pct Si high silicon steel: a promising soft magnetic material for sub-kHz application. *J. Magnet. Magnetic Mater.*, 2019, vol. 481, pp. 234–50.
2. T.N. Lamichhane, L. Sethuraman, A. Dalagan, H. Wang, J. Keller, and M.P. Paranthaman: Additive manufacturing of soft magnets for electrical machines—a review. *Mater Today Phys.*, 2020, vol. 15, 100255.
3. R. Liang, P. Yang, and W. Mao: Cube texture evolution and magnetic properties of 65 wt pct Si electrical steel fabricated by surface energy and three-stage rolling method. *J. Mag. Mag. Mater.*, 2018, vol. 457(2018), pp. 38–45.
4. X. Wang, Z. Liu, H. Li, and G. Wang: Microstructural evolution in warm-rolled and cold-rolled strip cast 6.5 wt pct Si steel thin sheets and its influence on magnetic properties. *J. Mag. Mag. Mater.*, 2017, vol. 433, pp. 8–16.
5. H.J. Xu, Y.B. Xu, H.T. Jiao, S.F. Cheng, R.D.K. Misra, and J.P. Li: Influence of grain size and texture prior to warm rolling on microstructure, texture and magnetic properties of Fe-6.5 wt pct Si steel. *J. Mag. Mag. Mater.*, 2018, vol. 453, pp. 236–45.
6. X. Shen, F. Meng, K.B. Lau, P. Wang, and C.H.T. Lee: Texture and microstructure characterizations of Fe-3.5 wt pct Si soft magnetic alloy fabricated via laser powder bed fusion. *Mater Charact.*, 2022, vol. 189, p. 112012.

7. Y. He and E.J. Hilinski: Textures of non-oriented electrical steel sheets produced by skew cold rolling and annealing. *Metals*, 2022, vol. 12(1), p. 17.
8. L. Fan, Y. Zhu, E. Yue, J. He, and L. Sun: Microstructure and texture evolution of ultra-thin high grade non-oriented silicon steel used in new energy vehicle. *Mater. Res. Express*, 2022, vol. 9(9), 096515.
9. H. Xu, Y. Xu, Y. He, H. Jiao, S. Yue, and J. Li: A quasi in-situ EBSD study of the nucleation and growth of Goss grains during primary and secondary recrystallization of a strip-cast Fe-65 wt pct Si alloy. *J. Alloys Compd.*, 2021, vol. 861, p. 158550.
10. M. Yasuda, K. Murakami, and K. Ushioda: Recrystallization behavior and formation of {411}<148> grain from α -fiber grains in heavily cold-rolled Fe-3%Si alloy. *ISIJ Int.*, 2020, vol. 60(11), pp. 2558–568.
11. J. Qin, J. Yang, Y. Zhang, Q. Zhou, and Y. Cao: Strong {100}<012>-{411}<148> recrystallization textures in heavily hot-rolled non-oriented electrical steels. *Mater. Lett.*, 2020, vol. 259, 126844.
12. M. Mehdi, Y. He, E.J. Hilinski, L.A.I. Kestens, and A. Edrissy: The evolution of cube ({001}<100>) texture in non-oriented electrical steel. *Acta Mater.*, 2020, vol. 185, pp. 540–54.
13. T.Y. Kim, T.W. Na, H.S. Shim, Y.K. Ahn, Y.K. Jeong, H.N. Han, and N.M. Hwang: Misorientation characteristics at the growth front of abnormally-growing Goss grains in Fe-3%Si steel. *Met. Mater. Int.*, 2021, vol. 27, pp. 5114–120.
14. M. Mehdi, Y. He, E.J. Hilinski, and A. Edrissy: Texture evolution of a 28 wt pct Si non-oriented electrical steel and the elimination of the {111}<ND> texture. *Metall. Mater. Trans. A*, 2019, vol. 50, pp. 3343–357.
15. S. Takajo, C.C. Merriman, S.C. Vogel, and D.P. Field: In-situ EBSD study on the cube texture evolution in 3 wt pct Si steel complemented by ex-situ EBSD experiment from nucleation to grain growth. *Acta Mater.*, 2019, vol. 166, pp. 100–12.
16. D. Hawezzy and S. Biroscia: Disparity in recrystallization of α - & γ -fibers and its impact on Cube texture formation in non-oriented electrical steel. *Acta Mater.*, 2021, vol. 216, 117141.
17. M. Sanjari, M. Mehdi, Y. He, E.J. Hilinski, S. Yue, L.A.I. Kestens, and A. Edrissy: Tracking the evolution of annealing textures from individual deformed grains in a cross-rolled non-oriented electrical steel. *Metall. Mater. Trans. A*, 2017, vol. 48, pp. 6013–26.
18. H.Z. Li, Z.Y. Liu, X.L. Wang, H.M. Ren, C.G. Li, G.M. Cao, and G.D. Wang: {114}<481> Annealing texture in twin-roll casting non-oriented 65 wt pct Si electrical steel. *J. Mater. Sci.*, 2017, vol. 52(1), pp. 247–59.
19. G. Zu, X. Zhang, J. Zhao, Y. Wang, Y. Cui, Y. Yan, and Z. Jiang: Analysis of {411}<148> recrystallisation texture in twin-roll strip casting of 4.5 wt pct Si non-oriented electrical steel. *Mater. Lett.*, 2016, vol. 180, pp. 63–67.
20. N. Zhang, P. Yang, and W. Mao: 001<120>-{113}<361> recrystallization textures induced by initial {001} grains and related microstructure evolution in heavily rolled electrical steel. *Mater. Charact.*, 2016, vol. 119, pp. 225–32.
21. C.X. He, F.Y. Yang, G. Ma, X. Chen, and L. Meng: {411}<148> texture in thin-gauge grain-oriented silicon steel. *Acta Metall. Sin. (English Lett.)*, 2016, vol. 29(6), pp. 554–60.
22. M. Sanjari, Y. He, E.J. Hilinski, S. Yue, and L.A.I. Kestens: Development of the {113}<uvw> texture during the annealing of a skew cold rolled non-oriented electrical steel. *Scrip. Mater.*, 2016, vol. 124, pp. 179–83.
23. H. Xu, Y. Xu, Y. He, S. Cheng, H. Jiao, S. Yue, and J. Li: Two-stage warm cross rolling and its effect on the microstructure, texture and magnetic properties of an Fe-65 wt pct Si non-oriented electrical steel. *J. Mater. Sci.*, 2020, vol. 55(26), pp. 12525–2543.
24. P. Governado, R.H. Petrov, J. Moerman, C. Barbatti, and L.A.I. Kestens: Recrystallization texture of ferrite steels: beyond the γ -fibre. *Mater. Sci. Forum*, 2012, vol. 702–703, pp. 790–93.
25. L. Kestens and S. Jacobs: Texture control during the manufacturing of nonoriented electrical steels. *Texture Stress Microstruct.*, 2008, vol. 2008, 173083.
26. P. Governado, R.H. Petrov, and L.A.I. Kestens: Recrystallized {311}<136> orientation in ferrite steels. *Scrip. Mater.*, 2012, vol. 66(9), pp. 623–26.
27. M. Sanjari, Y. He, E.J. Hilinski, S. Yue, and L.A. Kestens: Development of the {113}<uvw> texture during the annealing of a skew cold rolled non-oriented electrical steel. *Scrip. Mater.*, 2016, vol. 124, pp. 179–83.
28. P. Governado, R. Petrov, D. Ruiz, E. Leunis, and L. Kestens: Texture evolution in Si-alloyed ultra low-carbon steels after severe plastic deformation. *Adv. Eng. Mater.*, 2010, vol. 12(10), pp. 1077–81.
29. L. Kestens, J. Jonas, P. Van Houtte, and E. Aernoudt: Orientation selection during static recrystallization of cross rolled non-oriented electrical steels. *Text. Stress. Microst.*, 1996, vol. 26, pp. 321–35.
30. K. Verbeken, L. Kestens, and M. Nave: Re-evaluation of the Ibe-Lücke growth selection experiment in a Fe-Si single crystal. *Acta Mater.*, 2005, vol. 53(9), pp. 2675–682.
31. K.K. Alaneme and E.A. Okotete: Recrystallization mechanisms and microstructure development in emerging metallic materials: a review. *J. Sci.*, 2019, vol. 4(1), pp. 19–33.
32. F. Gao, Y. Chen, Q. Zhu, Y. Nan, S. Tang, Z. Cai, F. Zhang, W. Xue, X. Cai, F. Yu, and Z. Liu: Formation of recrystallization texture and its effect on deep drawability for high-purified ferritic stainless steel by two step cold rolling. *Mater. Des.*, 2023, vol. 226, 111679.
33. A. Després, J.D. Mithieux, and C.W. Sinclair: Modelling the relationship between deformed microstructures and static recrystallization textures: application to ferritic stainless steels. *Acta Mater.*, 2021, vol. 219, 117226.
34. F. Fang, J. Wang, J. Yang, Y. Zhang, Y. Wang, G. Yuan, X. Zhang, R.D.K. Misra, and G. Wang: Formation of η -oriented shear bands and its significant impact on recrystallization texture in strip-cast electrical steel. *J. Market. Res.*, 2022, vol. 21, pp. 1770–783.
35. J. Saha, R. Saha, and P.P. Bhattacharjee: Microstructure and texture development in CoCrNi medium entropy alloy processed by severe warm cross-rolling and annealing. *Intermetallics*, 2022, vol. 143, 107463.
36. W. Liu, Z. Liu, W. Luo, H. Liu, Q. Wang, and R. Zhang: Influence of Zr on grain orientation, texture, and mechanical properties in hot- and warm-rolled FeCrAl alloys. *Mater. Charact.*, 2022, vol. 183, 111602.
37. Y. Li, Z. Du, J. Fan, Y. Lv, Y. Lv, L. Ye, and P. Li: Microstructure and texture evolution in warm-rolled fine-grained tungsten. *Int. J. Refract. Metal. Hard Mater.*, 2021, vol. 101, 105690.
38. J. Saha, R. Saha, and P.P. Bhattacharjee: Microstructure and texture of severely warm-rolled and annealed coarse-grained CoCrNi medium entropy alloy (MEA): a perspective on the initial grain size effect. *J. Alloys Compd.*, 2022, vol. 904, 163954.
39. H.T. Jiao, Y. Xu, L.Z. Zhao, R.D.K. Misra, Y.C. Tang, M.J. Zhao, D.J. Liu, Y. Hu, and M.X. Shen: Microstructural evolution and magnetic properties in strip cast non-oriented silicon steel produced by warm rolling. *Mater. Charact.*, 2019, vol. 156, 109876.
40. S. Lee and B.C. De Cooman: Effect of warm rolling on the rolling and recrystallization textures of non-oriented 3% Si steel. *ISIJ Int.*, 2011, vol. 51(9), pp. 1545–552.
41. J. Jonas: Effects of shear band formation on texture development in warm-rolled IF steels. *J. Mater. Process. Technol.*, 2001, vol. 117(3), pp. 293–99.
42. R. Machado, A. Kasama, A. Jorge Jr., C. Kiminami, W.B. Fo, and C. Bolfarini: Evolution of the texture of spray-formed Fe-65 wt% Si-10 wt% Al alloy during warm-rolling. *Mater. Sci. Eng. A*, 2007, vol. 449, pp. 854–57.
43. H. Xu, Y. Xu, Y. He, S. Yue, and J. Li: Tracing the recrystallization of warm temper-rolled Fe-65 wt pct Si non-oriented electrical steel using a quasi in situ EBSD technique. *J. Mater. Sci.*, 2020, vol. 55, pp. 17183–7203.
44. X. Wang, W. Zhang, Z. Liu, H. Li, and G. Wang: Improvement on room-temperature ductility of 65 wt% Si steel by stress-relief annealing treatments after warm rolling. *Mater. Charact.*, 2016, vol. 122, pp. 206–14.
45. H. Yu, K. Ming, H. Wu, Y. Yu, and X. Bi: Ordering suppression and excellent ductility in soft-magnetic Fe-6.5 wt pct Si sheet by Hf addition. *J. Alloys Compd.*, 2018, vol. 766, pp. 186–93.
46. H. Dun, Y. Zhang, N. Wang, Y. Wang, F. Fang, G. Yuan, R.D.K. Misra, and X. Zhang: Effect of Σ 3 grain boundaries on microstructure and properties of oriented Fe-65 wt pct Si in twin-roll strip casting. *J. Mag. Mag. Mater.*, 2022, vol. 559, p. 169552.

47. F.J. Humphreys and M. Hatherly: *Recrystallization and Related Annealing Phenomena*, Elsevier Ltd, Oxford, 2004.
48. I. Samajdar, B. Verlinden, L. Kestens, and P.V. Houtte: Physical parameters related to the developments of recrystallization textures in an ultra low carbon steel. *Acta Mater.*, 1998, vol. 47(1), pp. 55–65.
49. R.K. Ray, J.J. Jonas, and R.E. Hook: Cold rolling and annealing textures in low carbon and extra low carbon steels. *Metall. Rev.*, 1994, vol. 39(4), pp. 129–72.
50. R.L. Every and M. Hatherly: Oriented nucleation in low-carbon steels. *Texture*, 1974, vol. 1(3), pp. 183–94.
51. R. Sandstrom: Subgrain growth occurring by boundary migration. *Acta Metall.*, 1977, vol. 25(8), pp. 905–11.
52. Y. Sha, C. Sun, F. Zhang, D. Patel, X. Chen, S. Kalidindi, and L. Zuo: Strong cube recrystallization texture in silicon steel by twin-roll casting process. *Acta Mater.*, 2014, vol. 76(9), pp. 106–17.
53. H. Jiao, Y. Xu, L. Zhao, R. Misra, Y. Tang, D. Liu, Y. Hu, M. Zhao, and M. Shen: Texture evolution in twin-roll strip cast non-oriented electrical steel with strong Cube and Goss texture. *Acta Mater.*, 2020, vol. 199(10), pp. 311–25.
54. O. Engler: On the influence of orientation pinning on growth selection of recrystallisation. *Acta Mater.*, 1998, vol. 46(5), pp. 1555–68.
55. D.J. Jensen: Growth rates and misorientation relationships between growing nuclei/grains and the surrounding deformed matrix during recrystallization. *Acta Metall. Mater.*, 1995, vol. 43(11), pp. 4117–29.
56. R. Saha and R.K. Ray: Effect of severe cold rolling and annealing on the development of texture, microstructure and grain boundary character distribution in an interstitial free (IF) steel. *ISIJ Int.*, 2008, vol. 48(7), pp. 976–83.
57. K. Verbeken, L. Kestens, and J. Jonas: Microtextural study of orientation change during nucleation and growth in a cold rolled ULC steel. *Scrip. Mater.*, 2003, vol. 48(10), pp. 1457–62.
58. T. Nguyen-Minh, J. Sidor, R. Petrov, and L. Kestens: Occurrence of shear bands in rotated Goss ($\{110\}$ / $\{110\}$) orientations of metals with bcc crystal structure. *Scrip. Mater.*, 2012, vol. 67(12), pp. 935–38.

Publisher's Note Springer Nature remains neutral with regard to jurisdictional claims in published maps and institutional affiliations.

Springer Nature or its licensor (e.g. a society or other partner) holds exclusive rights to this article under a publishing agreement with the author(s) or other rightsholder(s); author self-archiving of the accepted manuscript version of this article is solely governed by the terms of such publishing agreement and applicable law.